JOURNAL OF THERMOPHYSICS AND HEAT TRANSFER
Vol. 20, No. 4, October–December 2006

Convective and Radiative Heat Flux Prediction of Huygens's Entry on Titan

L. M. Walpot*
Advanced Operations and Engineering Services Group, 2332 KG Leiden, The Netherlands
L. Caillault†
Laboratoire EM2C, 92295 Châtenay-Malabry, France
R. C. Molina‡
ESA, 2200 AG Noordwijk, The Netherlands
C. O. Laux§
Laboratoire EM2C, 92295 Châtenay-Malabry, France
and
T. Blanquaert‖
ESA, 2200 AG Noordwijk, The Netherlands

DOI: 10.2514/1.20901

The present paper focuses on the convective and radiative heat flux predictions required for the post-delta Flight Acceptance Review consolidation of the Huygens entry profile and, in particular, the desired flight path angle at entry interface. This consolidation effort has concluded on the appropriateness of the probe's thermal protection system design under the nominal and dispersed entry conditions considered and has supported the positive decision for Huygens's release from its carrier, Cassini, in December 2004. The related predictions are based on the atmospheric model of Yelle as implemented during the Huygens recovery effort (2002–2004) by the companies Alcatel and European Aeronautic Defence and Space, Les Mureaux and subsequent variations thereof. The atmospheric model (with emphasis on chemical composition, gravity wave, and wind profiles) has been updated before probe release during the Titan flybys in October 2004 and the final preentry predictions reported here have been performed with the atmospheric model resulting from the observations recorded during the second Titan flyby and the preflight trajectory baselined during the delta Flight Acceptance Review in February 2004. The results obtained clearly support the appropriateness of the thermal protection system design and the decision for probe release.

Nomenclature

D = diffusion coefficient, $\mathrm{m^2/s}$
H = heat load, $\mathrm{MJ/m^2}$
k = Boltzmann constant, J/K
m = mass, kg
Q = heat flux, $\mathrm{W/m^2}$
T = temperature, K
t = time, s
γ = recombination coefficient
ρ = density, $\mathrm{kg/m^3}$

Subscripts

c = convective
r = radiative
s = species number

I Introduction

THE delta Flight Acceptance Review of the Huygens probe in February 2004 prompted the requirement to revisit the preflight aerothermal predictions on the basis of the improved knowledge of Titan's atmosphere. Also, improvements made in the physical modeling after the probe's design phase (in the early 1990s), were required to be used for this updated assessment.

Among the challenges posed by Huygens's aerothermal environment characterization, the atmospheric composition [1] of Titan (consisting mainly of diatomic nitrogen and up to 2.2% of methane) leads to the formation of CN in the shock layer, and this species strongly radiates in the violet and red systems. Radiation from CN is responsible for the major part of the heat flux to the probe and must therefore be factored in the probe's overall aeroheating.

Also important is the formation of hydrogen, which impacts the convective heating by diffusion. These issues are discussed in depth by Wright et al. [2].

The adoption of standard reaction rates (Nelson et al. [3] and Gökçen, [4]) of a self-consistent effective binary diffusion model (SCEBD) for the modeling of transport properties, properly accounting for the diffusion of hydrogen atoms, and the correct implementation of turbulence models have been of particular relevance in the aeroheating convergence effort. Both aspects are discussed and illustrated with the updated status at the end of the convergence process.

Furthermore, the converged flowfield data have been used with the code SPECAIR [5] to compute radiative heating, assuming a Boltzmann distribution of the excited electronic levels at a characteristic temperature taken as the vibrational temperature of the gas. The SPECAIR code has been validated in [5] by comparison of simulated and experimental spectra of the CN violet system and of the first negative system of N_2^+. CN violet is found to be the most intense emitter, followed by CN red, C_2 Swan, and, at early trajectory

---

Received 5 November 2005; revision received 24 February 2006; accepted for publication 12 February 2006.

[*] Research Scientist, Haagse Schouwweg 6G.

[†] Research Scientist, Ecole Centrale Paris, CNRS-UPR288, Grande Voie des Vignes.

[‡] Head, European Space Research and Technology Centre, Aerodynamics and Aerothermodynamics Unit HME-MEA, Keplerlaan 1.

[§] Professor, Ecole Centrale Paris, CNRS-UPR288, Grande Voie des Vignes.

[‖] Huygens System Engineering Manager, European Space Research and Technology Centre, Keplerlaan 1.

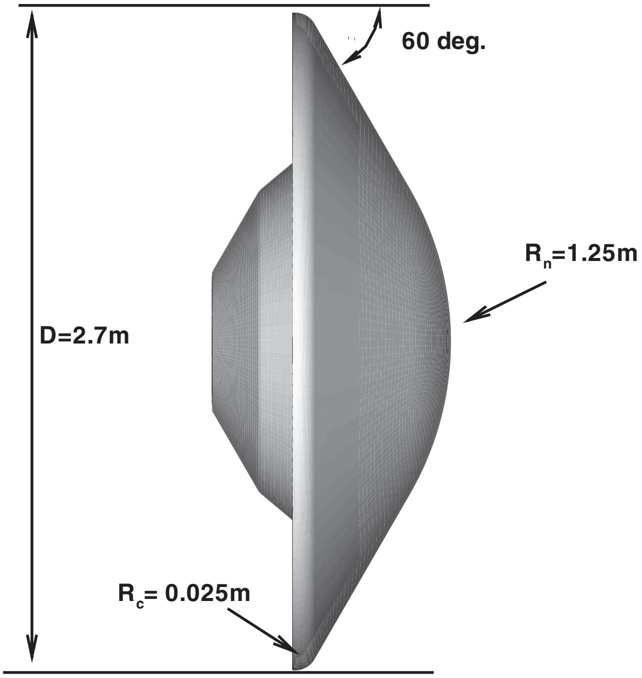

Fig. 1 Geometrical parameters of the Huygens probe.

points, by the N_2 first and second positives. Solutions of the one-dimensional (1-D) radiative transport equation along various lines of sight (including the stagnation streamline) show that the self-absorption by the plasma layer reduces the total emission by up to approximately 20%. The fine structure of the CN violet spectra (spin-splitting) must be taken into account to accurately determine self-absorption by CN violet. The resulting fluxes (convective and radiative) were then used to assess the thermal protection system (TPS) behavior. The feasibility of the mission was confirmed under the updated entry parameters and atmospheric composition.

The geometrical parameters of the Huygens probe (Fig. 1) taken into consideration for the analysis derived herein are: 2.7 m maximum decelerator diameter, 1.250 m nose radius, 60 deg cone angle, and a reference surface of 5.73 m^2.

II. Trajectories

In Table 1, four basic Yelle et al. [1] atmospheric models are considered (i.e., Yelle min, nom, max, and post-TA, respectively) and thereafter, variations of the reference models whereby the relative concentrations of N_2, CH_4, and Ar are modified according to the $[X_{N_2}, X_{CH_4}, X_{Ar}]$ appendage to the relevant models. For these variations, the resulting atmospheric density is within a small range centered at the corresponding Yelle submodel (e.g., both models 7 and 8 result in an atmospheric density close to that of the so-called Yelle max). Finally, the atmospheric model characterized after the second flyby, also called the "TA event" of 26 Oct 2004, and variations thereof with wind correction have been considered for the final verification of the probe's design.

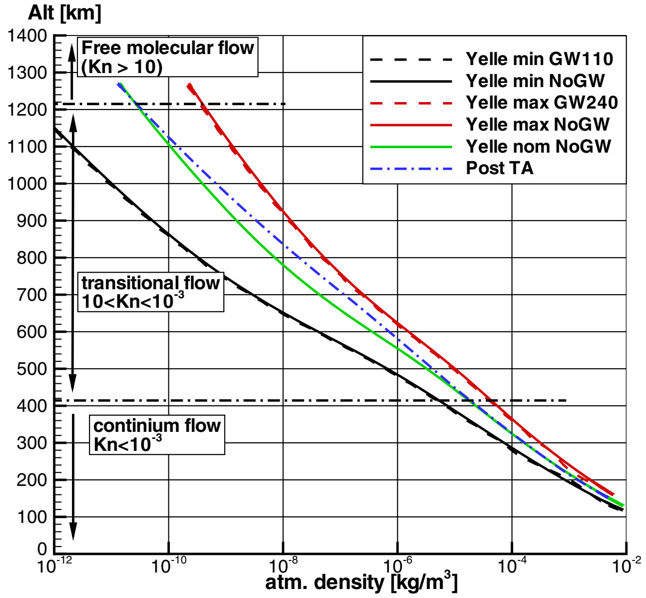

Fig. 2 Titan atmospheric density profiles.

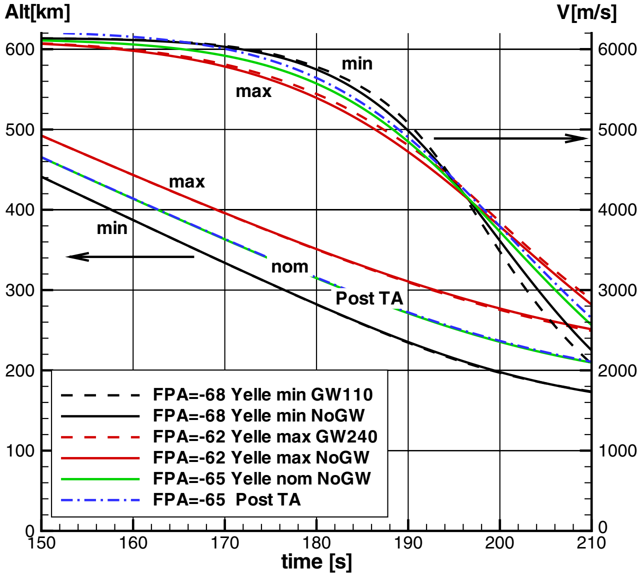

Fig. 3 Trajectories associated with the previous atmospheric models and FPA at EI, per Table 1.

Table 1 Definition matrix for Huygens entry conditions with mole fraction $[N_2 - CH_4 - Ar]$

1. Sensitivity to gravity wave perturbations
    1) Yelle min [95-5-0] -68 GW110
    2) Yelle min [95-5-0] -68 NoGW
    3) Yelle max [89-1-10] -62 GW240
    4) Yelle max [89-1-10] -62 NoGW
2. Sensitivity to CH_4
    5) Yelle min (A) [97-3-0] -68 NoGW
    6) Yelle min (B) [99-1-0] -68 NoGW
3. Sensitivity to argon
    7) Yelle max (A) [92-1-7] -62 NoGW
    8) Yelle max (B) [97-1-2] -62 NoGW
4. Nominal entry CH_4/N_2
    9) Yelle nom [95-3-2] -65 NoGW
    10) Yelle nom (A) [96-2-2] -65 NoGW
5. Post-TA entry with wind correction
    11) Post-TA [97.7-2.3-0] -65 NoGW
    12) Post-TA (A) [96.7-3.2-0] -65 NoGW
    13) Post-TA (B) [98.2-1.8-0] -65 NoGW

Additionally considered is occurrence of gravity waves and their phase, if relevant, which is referenced by the GW110, GW240, and NoGW qualifiers at the end of each case. The respective atmospheric density profiles vs altitude are depicted in Fig. 2.

In Table 1, the flight path angle (FPA) on the probe at the atmospheric entry interface (EI) is also referenced. FPA's at EI of −62, −65, and −68 deg have been considered, corresponding to shallow, nominal, and steep entry cases, respectively. Figure 3 summarizes the time evolution of altitude and relative velocity in the continuum regime (relevant to the occurrence of peak heating and before the descent landing system activation) for the cases outlined in Table 1.

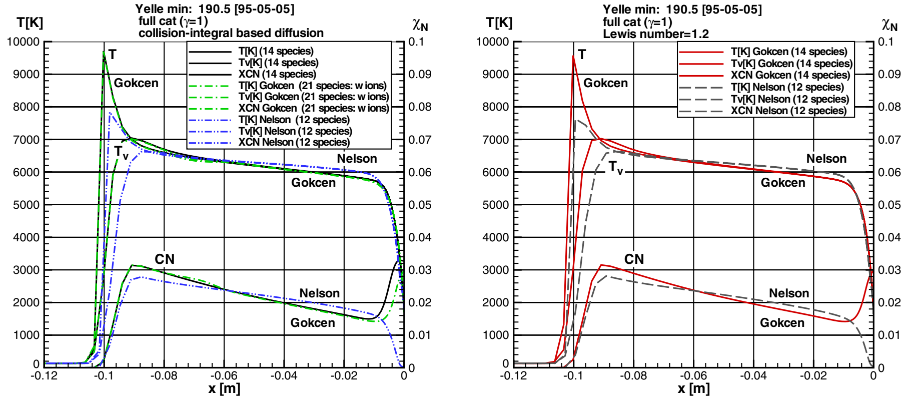

a) Collision-integral diffusion **b) Fixed Lewis number = 1.2**

Fig. 4 Influence of Nelson et al. [3] and Gökçen [4] (with and without ionization) on stagnation line temperatures and CN mole fraction with assuming different diffusion models at peak heat flux of the Yelle min FPA = −68 deg trajectory.

III. Numerical and Physical Modeling

The flowfield calculations are performed using the CFD code LORE [6]. LORE is a multiblock finite volume Navier–Stokes solver augmented with finite rate chemistry and thermal nonequilibrium effects. The convective fluxes are computed with a modified advection upwind split method (AUSM) scheme with a monotonic upwind-centered scheme for conservation laws (MUSCL) extrapolation to achieve second-order accuracy coupled with a van Albada limiter. Viscous fluxes are computed with second-order accuracy by central differencing. Time advancement to a steady-state solution is achieved using an alternating direction line Gauss–Seidel implicit relaxation method. LORE has been extensively validated against X-38 wind-tunnel test data [obtained at ONERA S3Ma, S4Ma, F4, Langley Research Center (LaRC) Mach 6, and Deutsche Zentrum für Luft-und Raumfahrt (DLR) HEG] and atmospheric reentry demonstrator (ARD) wind-tunnel data and flight results [6].

Flowfield data and convective heat fluxes on similar Titan trajectories have been cross-checked, in particular, with NASA Ames's Navier–Stokes code DPLR [7] and NASA Langley's code LAURA [8]. A thorough summary of the code calibration study between the latter three can be found in [9]. Each code employs different flux discretization and convergence acceleration methods, but has similar physical models for Titan entry, as agreed upon by a combined NASA/ESA Huygens aeroheating convergence working group (ACWG) at ESA headquarters in November 2004. In [9] it is concluded that all three codes are within 3% for both laminar and turbulent heating rates for Titan entry conditions covering the entire relevant hypersonic phase and excellent agreement is found on flowfield variables along the extracted stagnation lines.

Radiation heat fluxes can be contributed to the thermal and chemical nonequilibrium shock layer of Huygens entering Titan. The main radiator CN is formed in the shock layer, the amount of CN produced depends critically on the freestream methane concentration. The thermal nonequilibrium effects will drive the amount of radiation, as detailed later in this section. A total and a vibro-excitational-energy equation are solved. A Landau–Teller formulation is used to describe the exchange between the translational-rotational and vibrational-electronic, in which the relaxation times are obtained from Millikan and White [10], assuming simple harmonic oscillators. The vibrational temperatures of the molecules are taken from Gurvich et al. [11].

For the Huygens entry, analysis indicated that the amount of ionization is small enough to disregard its impact on convective and radiative heat fluxes, as shown in Fig. 4. Two finite rate models were employed to derive the data reported in Fig. 4: the Nelson et al. [3] model (CH_4, CH_3, CH_2, N_2, C_2, H_2, CH, NH, CN, N, C, H, and Ar) and a revised Titan reaction set of Gökçen [4], including an additional HCN species. In the dissociation reaction activation $T_a = \sqrt{TT_v}$, T is the translational-rotational temperature, and T_v is the vibrational-electronic temperature. Equilibrium constants are computed using a minimized Gibbs free energy. Thermodynamic properties are taken from Gordon and McBride [12].

Trajectories 1 to 10 have been computed using the Nelson et al. [3] model with a fixed Lewis number of 1.2, whereas trajectories 10 to 13 have been computed with Gökçen's [4]. In Fig. 4, the temperatures and CN mole fraction along the stagnation line are depicted at peak heat flux on trajectory Yelle min 68, which is found to occur at 190.5 s. The impact of the finite rate models is most noticeable in the immediate post-shock area, where the Gökçen model predicts higher temperatures and CN mole fraction than Nelson et al. It must be emphasized, though, that because most of the shock layer is in thermal equilibrium and chemical nonequilibrium, the increased post-shock temperature is a localized effect that barely affects the convective heating at the wall. Additionally, a negligible impact on the radiative heating can be anticipated from Fig. 4, because CN concentration is very similar for both models. This point shall be evaluated later in this section. In the boundary layer, the Gökçen model results in CN presence, whereas the Nelson et al. model predicts CN depletion (caused by the different exchange reactions forming CN), assuming a full catalytic wall. The impact of CN presence on convective heating is, however, also negligible here because its influence is comparatively small vs that of the efficient hydrogen diffusion predicted by diffusion based on collision integrals. Species viscosity is modeled by Gordon and McBride [12] and a Eucken formulation is used to compute the thermal conductivities. The SCEBD method [13,14] is used to model diffusion fluxes. Collision integrals are taken from [15] for most binary interactions, all other species are modeled using a modified Lennard–Jones potential. The influence of the models considered is illustrated in Fig. 5. Supercatalytic wall boundary conditions, in which the maximum enthalpy is recovered by forcing the freestream species N_2 and CH_4 to recombine, are also used and yield roughly a 5–10% heat flux increase. (Although in practice at the wall temperature, the CH_4 formation is questionable, the difference in heat flux is negligible.) The Lewis number variation from 1.2 to 1.4 also results in negligible heat flux variations. Instead of forcing the recombination to freestream species as in the supercatalytic assumption, the surface catalysis can be modeled by using first-order reaction rates for N_2 and H_2 recombination. In the latter case, a so-called full catalytic wall results with a recombination coefficient γ_s set to 1. The mass flux at the wall can then be related to the rate of diffusion toward the surface, following

$$\rho D_s \frac{\partial c_s}{\partial y} = \gamma_s \rho_s \sqrt{\frac{kT_w}{2\pi m_s}} \tag{1}$$

This results in a convective stagnation heat flux decrease of around 7% between the super and the full catalytic assumptions. The adoption of a collision–integral-based diffusion vs a constant Lewis number formulation further increases the stagnation convective heat

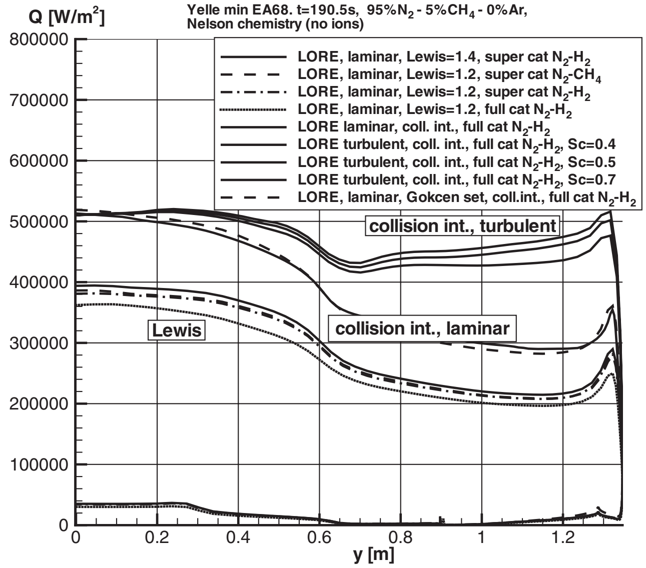

Fig. 5 Influence of diffusion modeling on convective heat flux distribution at peak heat flux of the Yelle min FPA = −68 deg trajectory.

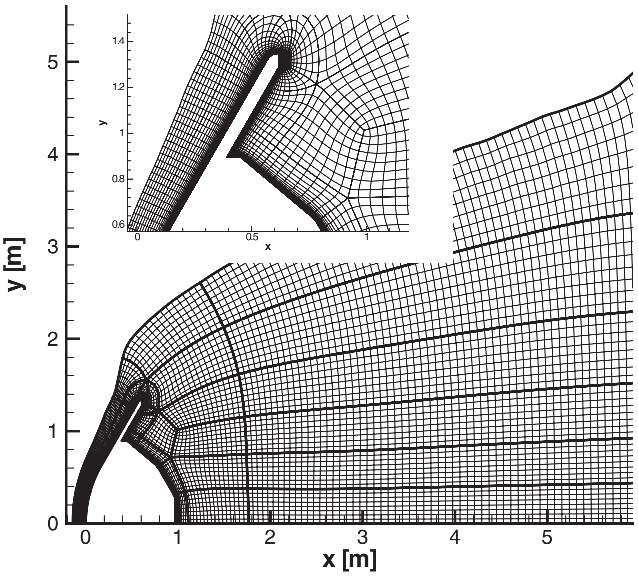

Fig. 6 Baseline computational mesh of 34 blocks (undoubled ±16 kcell).

flux by 25%. This ratio is increased to 50% in the midcone region. Accordingly, a constant correction factor for stagnation point heating of 1.25 has been applied to trajectories 1 to 10, which were computed with a constant 1.2 Lewis number in order to compensate for the identified deficit. It is shown later that such a correction is suitable for the whole trajectory range by comparison between the corrected constant Lewis computations and the collision-based diffusion results.

Turbulence is modeled using a compressible Baldwin–Lomax model [16] with standard compressibility corrections [17], and with turbulent Schmidt numbers of 0.4, 0.5, and 0.7, respectively. It can be observed that the turbulent Schmidt number influence is in the order of 8% at the flank, whereas the Schmidt number 0.5 results in comparable heating at the flank and stagnation points. The use of the algebraic turbulence model resulted from a consensus reached in the NASA/ESA Huygens ACWG because of the reasonable confidence in the use of the model for an attached flow for hypersonic flows and substantiated by its satisfactory performance at predicting convective turbulent heating in close agreement with wind-tunnel data obtained in LaRC Mach 6 [6,18] and Mach 10 [19] facilities.

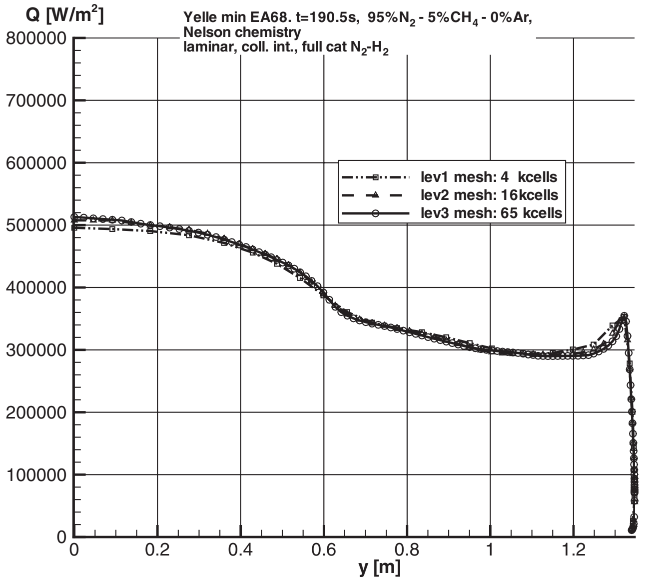

Fig. 7 Typical grid convergence on convective heat flux at the Yelle min FPA = −68 deg trajectory at 190.5 s.

Finally, a radiative equilibrium boundary condition has been implemented with an emissivity of 0.85, an acceptable assumption based on the carbonaceous nature of the charred thermal protection system.

Grid convergence has been established by performing the previous computations on the baseline mesh consisting of 34 blocks; $\pm 65,000$ cells with roughly 100 points in the normal direction on the front shield, of which roughly 50 points are located in the boundary layer; and a wall spacing with a cell Reynolds number less than 2. The grid independence of heat flux is then checked for each case by doubling/undoubling the mesh density. The undoubled mesh is shown in Fig. 6 and a typical convective heat flux in Fig. 7, converged within 3%.

The flowfield data obtained previously serve as input to compute the uncoupled radiation heat fluxes. The analysis of the radiative aerothermal environment of the Huygens probe was performed with the SPECAIR code. Near the shock front, the internal level populations should be obtained using a collisional-radiative model, but no experimentally validated collisional-radiative model was available for this mission to assess these populations in the nonequilibrium region. Therefore, the excited states of atoms and molecules were assumed to follow a Boltzmann distribution. Such a distribution is often considered to provide an upper limit of the density of the internal level populations. This approximation was tested for two conditions: those of a shock tube experiment and Huygens's entry conditions. In Bose et al. [20], the heat flux resulting from computations under Boltzmann distribution assumptions tend to overestimate the heat flux measured from their shock tube facility in an N_2/CH_4 rarefied environment assumed to be representative of the peak heating conditions of a Titan aerocapture trajectory. On the other hand, Magin et al. [21] have carried out nonequilibrium radiation modeling for Huygens's entry: for high shock-layer pressures of around 9662 Pa, the excited states are close to Boltzmann distribution populations. Thus, the Boltzmann distribution assumption is reasonable, or at least conservative, for application in this pressure range.

For all radiative heating computations presented here, the rotational, vibrational, and electronic levels have been assumed to follow Boltzmann distributions at the gas temperature $T_{\mathrm{rot}} = T_{\mathrm{gas}}$, the vibrational temperature and, again, the vibrational temperature $T_{\mathrm{elec}} = T_{\mathrm{vib}}$, respectively. The first assumption is reasonable, owing to fast collisional coupling between rotation and translation. The second assumption follows the recommendations of Park [22] when no experimentally validated vibrational-electronic state-specific collisional-radiative model is available. With these assumptions, the

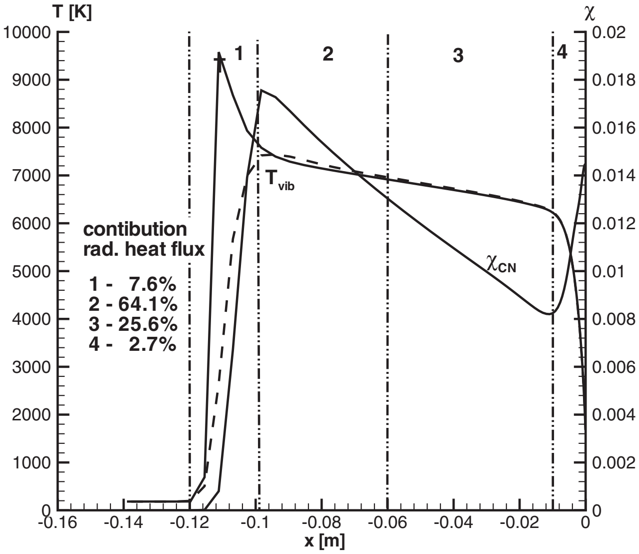

Fig. 8 Temperatures, CN mole fraction, and spectral emission coefficient distribution along the stagnation line at 191 s, trajectory 11.

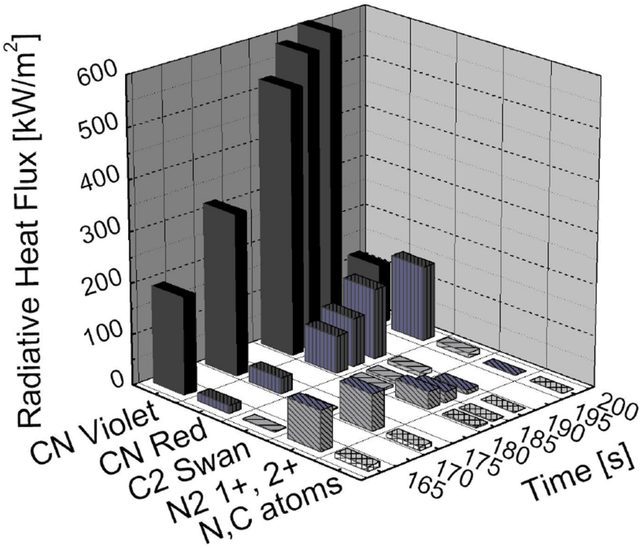

Fig. 9 Apportionment of the radiative components of the individual species to the total radiative heat flux.

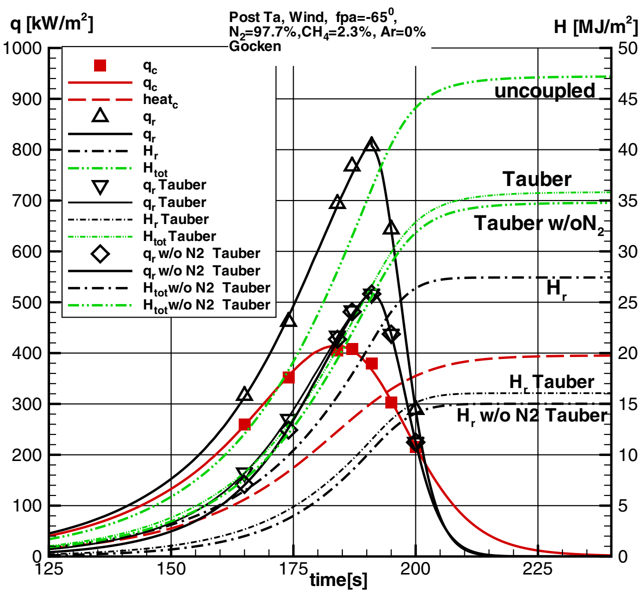

Fig. 10 Relief (coupling and N_2 quenching) on the post-TA atmosphere.

maximum amount of radiation is emitted in the thermal equilibrium region, where T_{vib} is slightly higher than T, as shown in Fig. 8, which presents the radiative contribution of the relaxation zone 1 of the thermal equilibrium zones 2 and 3 and of the boundary layer zone 4, for the point at 191 s of the post-TA wind 2.2 trajectory.

In the present uncoupled flowfield/radiation approach, SPECAIR uses LORE's thermochemical profiles of the shock layer to compute line-by-line emission and absorption. The spectral resolution used for computations plays an important role. Converged radiative heating results are obtained with SPECAIR when spectral resolution exceeds 350 points per nm. Thus, for all computations, a spectral resolution of 400 points per nm has been used, except in the spectral domain of the main radiator system CN violet, where a resolution of 1000 points per nm was taken. For the computations presented in the following sections, all transitions listed in Table 2 are considered, unless explicitly specified otherwise.

SPECAIR solves the transport equation along a line of sight using a 1-D tangent slab method. The 1-D tangent slab approximation is especially relevant for radiation assessment in the stagnation region of the flowfield, where gradients are mainly in the direction normal to the probe's surface. A correction factor $\alpha = 0.75$ is then applied to the 1-D radiative heat flux values, to account for 3-D effects due to the probe's surface curvature [7]. The radiative database used in SPECAIR is described by Laux [5].

A detailed analysis of the radiative heating at the stagnation point for several trajectories has been performed in order to estimate the contribution of all individual species, the effect of absorption, and the effect of spin-splitting. The conclusions obtained for the trajectory post-TA (B) FPA = −65 deg; NoGW are presented in the next section.

As shown in Fig. 9, CN has, by far, the largest contribution to the heat flux. As time increases, the relative contribution of CN violet radiation decreases and the contribution of CN red increases. C_2 Swan radiation rises with time but its contribution remains negligible. The first and second positive systems of N_2 contribute at the early times of the trajectories, then become negligible. The radiation of N, C, and NH is negligible.

Table 2 Summary of transitions

Species	Transitions considered in SPECAIR
CN	Violet (B-X) and red (A-X)
N_2	1st +(B-A), 2nd +
NH	A-X
C_2	Swan (d-a)
N	All transitions
C	All transitions

N_2 produces radiation at the early times of the trajectories. But our assumption of a Boltzmann distribution for the emitting N_2 states is debatable because excited states of N_2 are easily quenched by other molecules present in Titan's atmosphere. It is acknowledged that there is a lack of data on the quenching reaction of N_2^* under Huygens's entry conditions. However flowfield/radiation coupling tends to reduce the N_2 radiation by reducing post-shock T_{vib} [7].

IV. Results

The effect of modeling the coupled radiation relief by means of the Tauber–Wakefield correlation [23] is exemplified by the results of Fig. 10, where the reduction in peak heating and integrated heat load at stagnation point is evaluated for the post-TA atmosphere and a nominal FPA at EI of −65 deg. Though the additional effect of N_2 quenching has been incorporated, its magnitude has been found to be comparatively minor for all trajectories with less than 5% variation of the total heat load. On the contrary, a sizeable 25% reduction in integrated heating is found by virtue of radiation coupling/nonadiabatic effects modeling. In spite of the simplification

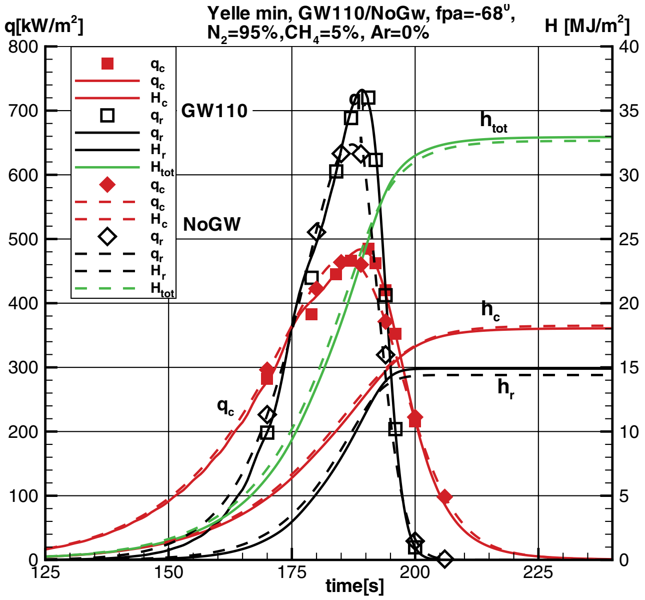

Fig. 11 Stagnation heat flux and heat load sensitivity to gravity waves perturbations for the Yelle min trajectory.

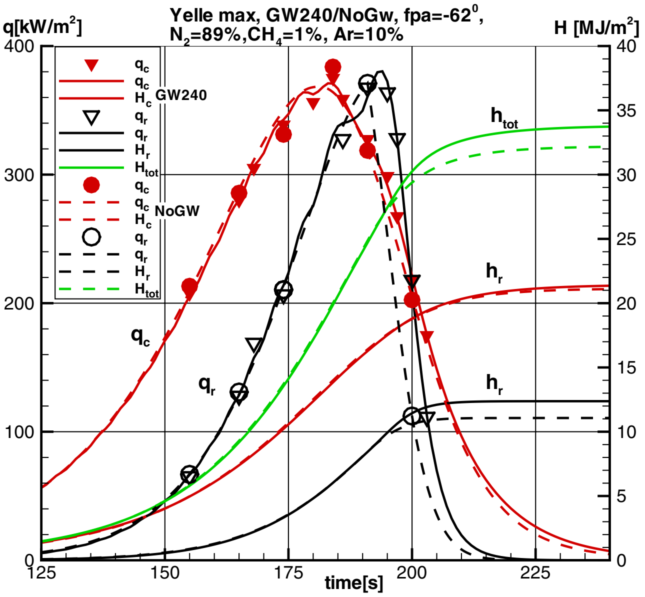

Fig. 12 Stagnation heat flux and heat load sensitivity to Gravity waves perturbations for the Yelle max trajectory.

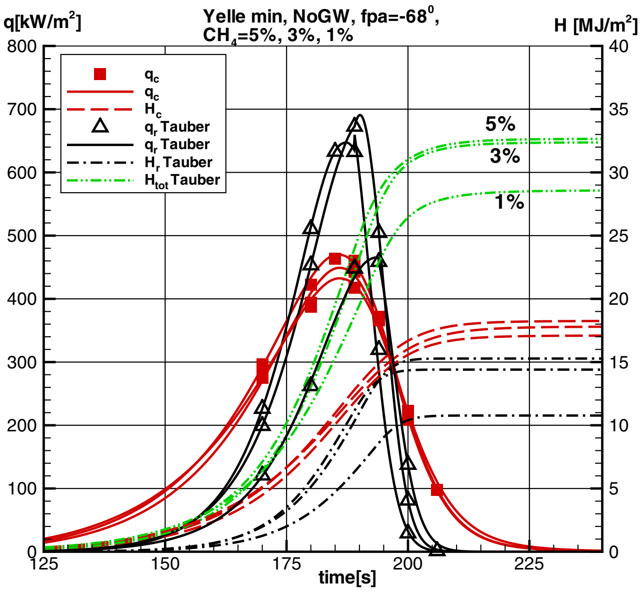

Fig. 13 Stagnation heat flux and heat load sensitivity to CH_4 variations (1 and 3%) for the Yelle min NoGW trajectory.

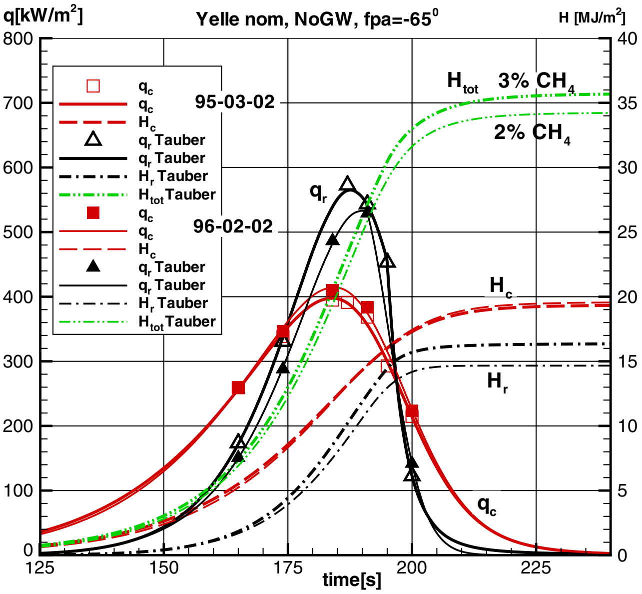

Fig. 14 Stagnation heat flux and heat load sensitivity to CH_4 variations (2 and 3%) for the Yelle nom NoGW trajectory.

of the radiation cooling through the use of the Tauber–Wakefield ansatz, the results obtained are fully compatible with those provided by a more elaborate, fully coupled methodology [7].

The heat flux and heat load histories are documented after splining of the computed points by a least-squares fit, which allows suitable correlations applicable over the whole trajectory to be derived.

Yelle min 68 and Yelle max 62 have been selected as the limiting cases for the evaluation of gravity wave impact on the stagnation point peak heating along the trajectories. The influence for both convective and radiative components has been documented in Figs. 11–13, with the radiative component being derived by the previously outlined uncoupled Boltzmann methodology with 1-D transport and subsequent Tauber–Wakefield correction [23] to account for coupling relief effects. On the other hand, the convective heating relief due to coupling has not been modeled. It is found that for both trajectories, the impact of gravity wave occurrence on the stagnation point heat flux and heat load is negligible. Additionally, in spite of the different atmospheric composition (CH_4 content, in particular) and FPA at the entry interface, the total heat load is comparable. However, a significant reduction of peak heating on Yelle max 62 vs Yelle min 68 occurs, with a maximum heat flux ratio of about 1.56.

The noticeable reduction in peak heating for the radiative component (and in a lesser proportion for convective heating) could be tentatively attributed to either a reduced FPA at EI, or a different atmospheric composition with reduced CH_4 content, or both. In a further investigation of the separate effect of reduced CH_4 concentration, it is found that the main contributor to the heat flux reduction is indeed the atmospheric composition, with the relief by FPA at EI variation being of lower magnitude. This fact is supported by the results shown on Fig. 13, where CH_4 concentrations of 1, 3, and 5% are investigated, exhibiting a considerable reduction in heat load and peak heating of 1 vs 3% with a less marked effect when comparing the 3 and 5% cases.

A similar investigation was carried out for the nominal entry case (Yelle nom 65 NoGW) for 2 and 3% CH_4 concentration, respectively (3% CH_4 is the nominal methane content for the Yelle atmospheric model). A reduction of 13% in heat load is achieved, mainly due to the radiative component (see Fig. 14).

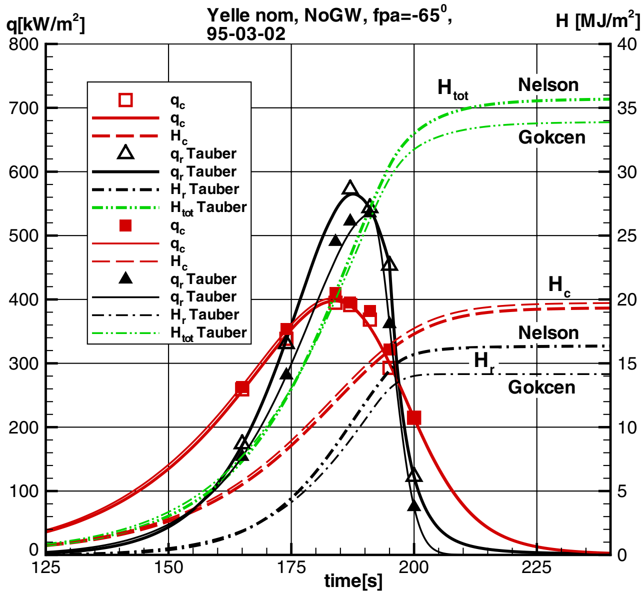

Fig. 15 Stagnation heat flux and heat load sensitivity to Nelson et al. [3] and Gökçen [4] for the Yelle min NoGW trajectory.

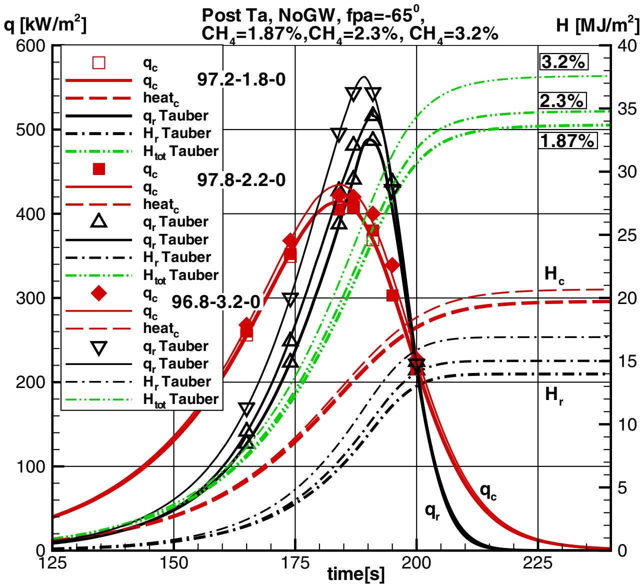

Fig. 17 Stagnation heat flux and heat load sensitivity to CH_4 variations (1.87 and 3.2%) for the post-TA trajectory.

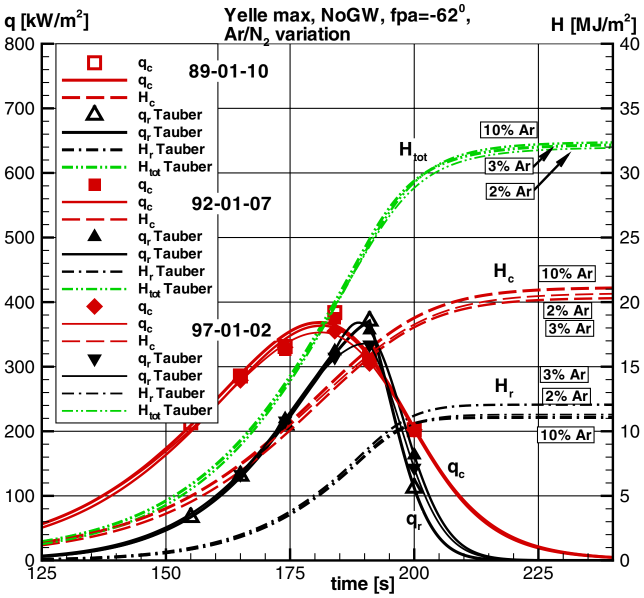

Fig. 16 Argon sensitivity on the Yelle max NoGW trajectory.

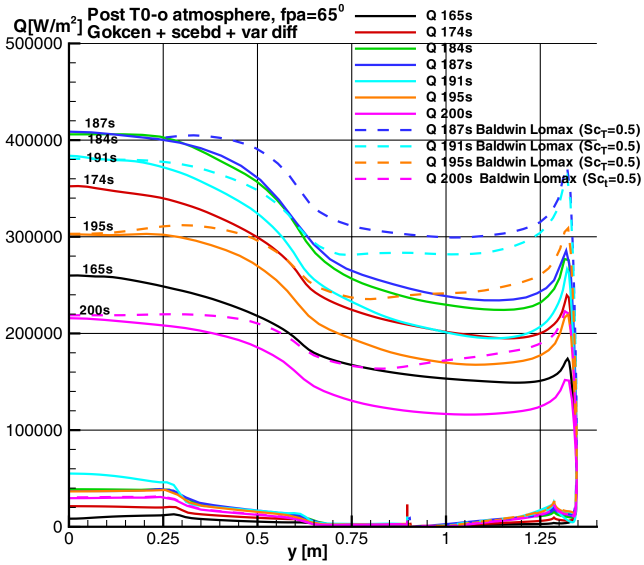

Fig. 18 Stagnation heat flux for the post-TA trajectory.

As previously mentioned, the computations have been performed with the Nelson et al. [3] kinetics model, and a constant Lewis number of 1.2. A 25% correction on convective heat flux was applied in order to match the results of the more elaborate collision–integral-based diffusion modeling. A thorough cross-check has been performed for the nominal entry case between both approaches, which is illustrated in Fig. 15, where excellent agreement on the convective component can be noticed over the entire trajectory, and a small lowering of the radiative heating is observed. This results in a slight reduction in heat load of the Gökçen [4] model with respect to Nelson et al.

Argon sensitivity has been examined in Fig. 16 on the Yelle max trajectory that exhibits the largest amount of argon (10%). A reduction of the argon content from 10% toward 7 and 2% revealed negligible changes in both radiative and convective heat fluxes.

The methodology applied thus far has been implemented for the updated post-TA atmospheric data after the second Titan flyby on 26 October 2004 (two months before the probe release from the Cassini spacecraft). The similarity in chemical composition is reflected in the comparable heating and heat load figures obtained after comparison with the Yelle nom 65 NoGW (i.e., in the order of $35\ \mathrm{MJ/m^2}$ for both cases, see Fig. 17).

The results presented so far concern primarily the stagnation point region. An assessment of the full forebody heating distribution has been required to ascertain the adequacy of the decelerator TPS architecture. This effort is reflected in Figs. 18 and 19, where the convective heating distribution along a meridian line on the heat shield and the heat flux/heatload history for the midcone and flank regions are shown.

In Fig. 18, the convective heating distribution on the heat shield for different times along the trajectory is documented for selected cases where the computed Re_θ/M_e exceeds the 150 value at the flank. In such cases, a fully turbulent flow is assumed over the entire front shield. A compressible Baldwin–Lomax model is then used to provide the turbulent heating levels required for midcone and flank TPS dimensioning.

As can be seen in Fig. 19, the heat loads at midcone and flank do not exceed that of the stagnation point, even after taking into consideration the turbulent transition.

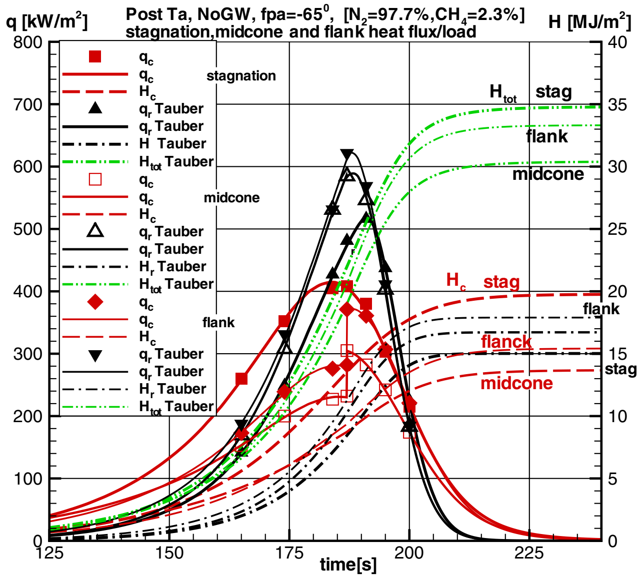

Fig. 19 Heat flux and heat load on stagnation, midcone, and flank for the post-TA trajectory.

V. Conclusion

An extensive analytical work based on advanced accepted methodology has been performed after the delta Flight Acceptance Review for the consolidation of the aerothermal environment of the Huygens probe and to support the go-ahead decision for its release from the Cassini carrier vehicle. A TPS response analysis with the heating results compiled here has been performed by the Huygens project, pointing to a clear survivability of the probe from the aerothermal standpoint.

The study has highlighted the importance of implementing a suitable spectral resolution and spin-splitting for the accurate evaluation of the radiative component (involving both emission and absorption phenomena).

The impact of CH_4 concentration on the final heat flux and heat load levels has been shown to be crucial, whereas that of argon is of lesser importance.

The isolated effect of flight path angle variation in the -68 to -62-deg range has been found to be of secondary importance on the peak heating and to be negligible for the integrated heat loads.

Gravity wave impact has proven quite irrelevant, as has the chemical kinetic modeling where only minor variations of the heating parameters have been observed. On the other hand, quite a large influence of the accurate modeling of the diffusion properties, properly accounting for the diffusion of H atoms in the boundary layer, has been noted, with the more sophisticated models resulting in increased convective heating levels.

The consideration of the relief provided by radiative coupling/nonadiabatic effects has proved essential at lowering the thermal input to the probe. The underlying radiative heating results from a conservative, experimentally validated Boltzmann approach that provides a reasonable upper bound for the heating estimates derived herein. This approach was deliberately selected to bracket the heating values between the less conservative assessments (such as the quasi-steady-state paradigm applied during the design phase of the Huygens probe) and the more classical, consolidated methodology.

Finally, turbulent heating has been considered on the heat shield with emphasis on the midcone-to-flank region, based on Re_θ transition criteria. The resulting heat flux has been shown to never exceed stagnation point values, and its effect on the integrated heat load has been shown to be of secondary importance.

In the work presented, the coupling between the flowfield and the injected products from the ablative AQ60 heat shield, as well as the potential radiation absorption/shielding effects of the injected material and the charred layer, have not been considered. These effects are anticipated to be beneficial as a source of heat flux relief and should be quantified for the design of future, optimized entry vehicles. Additionally, the plausible impact of nonequilibrium effects on the radiation levels has not been evaluated, as opposed to the Boltzmann equilibrium approach implemented here. Such effects are potentially relevant in the low-density environment encountered during the early phase of entry. It must be pointed out, however, that validation material for these advanced models is scarce and that reliable models have yet to be confronted by trustworthy ground and flight experimental data.

Acknowledgments

The authors thank Mike Wright of the NASA Ames Research Center for his elaborate help and support on the diffusion modeling and Naru Takashima of NASA Langley Research Center. Additionally, the authors would like to thank Anne Bourdon of EM2C for the extensive support on the radiation. Finally, J. P. Lebreton, Huygens project manager at ESA-ESTEC, the inexhaustible drive behind this project and without whose patronage this effort would not have been possible.

References

[1] Yelle, R. V., Strobel, D. F., Lellouch, E., and Gautier, D., "Engineering Models for Titan's Atmosphere," ESA Paper SP-1177, Aug. 1997.

[2] Wright, R., Hollis, B., Bose, D., and Walpot, L., "Post Flight Aerothermal Analysis of Huygens Probe," ESA Paper WPP-263, 2005.

[3] Nelson, H. F., Park, C., and Whiting, E., "Titan Atmospheric Composition by Hypervelocity Shock Layer Analysis," *Journal of Thermophysics and Heat Transfer*, Vol. 5, No. 2, April–June 1991, pp. 157–165.

[4] Gökçen, T., "CH_4-Ar Chemical Kinetic Model for Simulations of Atmospheric Entry to Titan," AIAA Paper 2004-2469, June 2004.

[5] Laux, C., "Optical Diagnostics and Radiative Emission of Air Plasmas," Ph.D. Thesis, Stanford Univ., Stanford, CA, 1993.

[6] Walpot, L., "Development and Application of a Hypersonic Flow Solver," Ph.D. Thesis, Delft Univ. of Technology, The Netherlands, May 2002.

[7] Wright, M., Bose, D., and Olejniczak, J., "The Impact of Flowfield-Radiation Coupling on Aeroheating for Titan Aerocapture," AIAA Paper 2004-0484, 2004.

[8] Cheatwood, F., and Gnoffo, P., "Users Manual for the Langley Aerothermodynamic Upwind Relaxation Algorithm (LAURA)," NASA TM-4764, 1996.

[9] Wright, M., Olejniczak, J., Walpot, L., Raynaud, E., Magin, T., Caillaut, L., and Hollis, B., "A Code Calibration Study for Huygens Entry Aeroheating," AIAA Paper 2006-0382, 2006.

[10] Millikan, R. C., and White, D. R., "Systematics of Vibrational Relaxation," *Journal of Chemical Physics*, Vol. 39, No. 12, Dec. 1963, pp. 3209–3213.

[11] Gurvich, L. V., Veyts, I. V., and Alcock, C. B., *Thermodynamic Properties of Individual Substances*, Vol. 1, Part 2, Hemisphere, New York, 1989.

[12] Gordon, S., and McBride, B., "Computer Program for Calculation of Complex Chemical Equilibrium Compositions, Rocket Performance, Incident and Reflected Shocks, and Chapman-Jouguet Detonations," NASA SP-273, 1976.

[13] Ramshaw, J., "Self-Consistent Effective Binary Diffusion in Multicomponent Gas Mixtures," *Plasma Chemistry and Plasma Processing*, Vol. 11, No. 3, 1991, pp. 395–402.

[14] Gupta, R. N., Yos, J., Thompson, R., and Lee, K., "A Review of Reaction Rates and Thermodynamic Transport Properties for an 11-Species Air Model for Thermal and Chemical Nonequilibrium Calcluations to 30000 K," NASA RP-1232, 1990.

[15] Stallcop, J. R., Partridge, H., and Levin, E., "Effective Potential Energies and Transport Cross Sections for Interactions of Hydrogen and Nitrogen," *Physical Review A*, Vol. 62, No. 6, 2000, pp. 1–15.

[16] Baldwin, B., and Lomax, H., "Thin Layer Approximation and Algebraic Model for Separated Turbulent Flows," AIAA Paper 78-0257, 1978.

[17] Brown, J., "Turbulence Model Validation for Hypersonic Flows," AIAA Paper 2002-3308, 2002.

[18] Horvath, T., and Fitzgerald, S., “X-38 Experimental Aerothermodynamics,” AIAA Paper 2000-2685, 2000.

[19] Berry, S. A., Horvath, T. J.Weilmuenster, K. J., Alter, S. J., and Merski, N. R., “X-38 Experimental Aeroheating At Mach 10,” AIAA Paper 2001-2828, 2001.

[20] Bose, D., Wright, M., Bogdano, D., Raiche, G., and Allen, G. A., Jr., “Modeling and Experimental Validation of CN Radiation Behind a Strong Shock Wave,” AIAA Paper 2005-768, 2005

[21] Magin, T., Caillault, L., Bourdon, A., and Laux, C., “Nonequilibrium Radiation Modeling for Huygens Entry,” ESA Paper WPP-263, 2005.

[22] Park, C., “Nonequilibrium Air Plasma NEQAIR Program: Users Manual,” NASA TM-86707, 1985.

[23] Tauber, M., and Wakefield, R., “Heating Environment and Protection During Jupiter Entry,” *Journal of Spacecraft and Rockets*, Vol. 8, No. 3, 1971, pp. 630–636.